A simplified mathematical model for heating-induced thermal runaway of lithium-ion batteries

Haodong Chen,[1] Jonathan E. H. Buston,[2] Jason Gill,[2] Daniel Howard,[2] Rhiannon C. E. Williams,[2] Elliott Read,[2] Ahmed Abaza,[3] Brian Cooper[3] and Jennifer X. Wen[1, z]

[1]Warwick FIRE, School of Engineering, University of Warwick, Library Road, Coventry, CV4 7AL, UK

[2]The Health and Safety Executive Science and Research Centre, Harpur Hill, Buxton, SK17 9JN, UK

[3]Jaguar Land Rover Limited, Abbey Road, Whitley, Coventry, CV3 4LF, UK.

Abstract

The present study aims to develop a simplified mathematical model for the evolution of heating-induced thermal runaway (TR) of lithium-ion batteries (LIBs). This model only requires a minimum number of input parameters, and some of these unknown parameters can be obtained from accelerating rate calorimeter (ARC) tests and previous studies, removing the need for detailed measurements of heat flow of cell components by differential scanning calorimetry. The model was firstly verified by ARC tests for a commercial cylindrical 21700 cell for the prediction of the cell surface temperature evolution with time. It was further validated by uniform heating tests of 21700 cells conducted with flexible and nichrome wire heaters, respectively. The validated model was finally used to investigate the critical ambient

[z]Corresponding author

E-mail address: Jennifer.wen@warwick.ac.uk

temperature that triggers battery TR. The predicted critical ambient temperature is between

127 °C and 128 °C. The model has been formulated as lumped 0D, axisymmetric 2D and full

3D to suit different heating and geometric arrangements and can be easily extended to predict

the TR evolution of other LIBs with different chemsitry and cathode materials. It can also be

easily implemented into other computational fluid dynamics (CFD) code.

Keywords: Thermal runaway; Lithium-ion battery safety; Mathematical model; Accelerating

rate calorimeter test; External heating; 21700 cell.

Nomenclature

A	pre-exponential factor (s^{-1}) or surface area (m^2)
Bi	Biot number
c	normalised amount of reactant
C_p	specific heat capacity (J kg^{-1} K^{-1})
E	activation energy (J mol^{-1})
h	heat transfer coefficient (W m^{-2} K^{-1})
H	reaction heat per unit mass (J kg^{-1}) or height (m)
k	thermal conductivity (W m^{-1} K^{-1})
L_c	characteristic length (m)
m	mass (kg)
n	reaction order
$\boldsymbol{n}$	normal vector
P	power (W)
$\boldsymbol{q}$	conductive heat flux vector (W m^{-2})
$\dot{Q}$	heat generation/dissipation rate (W)
r	radius of the cell (m)

R	gas constant (J mol^{-1} K^{-1})
t	time (s)
T	temperature (K)
V	volume (m^3)

Greek

α	fractional degree of conversion
ε	surface emissivity
η	correction factor
ρ	density (kg m^{-3})
σ	Stefan-Boltzmann constant (W m^{-2} K^{-4})

Subscripts

0	initial
∞	ambient
avg	average
max	maximum
diss	heat dissipation
gen	heat generation
i	I and II
r, x, y, z, φ	Directions

1. Introduction

The fast development of electric vehicles (EVs) has fuelled the demand for high energy density LIBs. This brings increasing attention to the potential fire and explosion hazards due to LIB thermal runaway (TR)[1], which is generally triggered by a series of continuous chain reactions until reactants are exhausted. The mechanism of TR has been reviewed in detail in some recent publications.[2-5] The thermal behaviour of LIBs can be described by three characteristic temperatures based on the results of hundreds of accelerating rate calorimeter (ARC) tests; the onset temperature, trigger temperature and maximum temperature.[6] The onset temperature mainly depends on the decomposition temperature of the solid electrolyte interphase (SEI). From onset temperature to maximum temperature, there is a lot of exothermic reactions that occur inside a cell. These exothermic reactions are mainly from the SEI decomposition, the reaction of electrolyte with anode/cathode material and binder, cathode material decomposition, electrolyte decomposition and Joule heat generated by internal short circuit (ISC).[2, 3] Therefore, understanding the TR mechanism and predicting its behaviour is of vital importance to setting an early warning signal for battery thermal management systems and developing effective measures to delay or avoid TR.

Numerous efforts have been directed towards developing mathematical models to predict TR behaviour since 1999. Richard and Dahn[7] studied the thermal stability of lithium intercalated mesocarbon microbead (MCMB) material in an electrolyte by measuring the rate of its self-heating using ARC. They proposed two mechanisms to explain the heat generated by chemical reactions between the lithiated carbon and $LiPF_6$ ethylene carbonate/diethyl carbonate electrolyte. The metastable components of SEI firstly decomposed to the stable products and this is followed by the formation of the new SEI resulting from the reaction between the intercalated Li and the electrolyte.[7, 8] They firstly developed a mathematical model to predict the self-heating of this anode material in the electrolyte at elevated temperatures.

Based on this, Hatchard et al.[9] developed a one-dimensional (1D) model to predict the onset temperature of TR of $LiCoO_2$/graphite cells exposed to a constant temperature oven. Although the model captured well the oven test results without TR, it failed to predict the high-temperature behaviour with sufficient accuracy as the complete exothermic reactions of cathode and electrolyte decomposition were not included. Spotnitz and Franklin[10] summarised the important exothermic reactions of cell components, which not only included the above mentioned reactions, but also the reaction of lithiated carbon with a binder, electrolyte decomposition, cathode material decomposition, and others. They developed a 1D model to analyse quantitatively the heat contribution of individual reactions and applied it to different abuse tests. Kim et al.[11] extended the 1D model of Hatchard et al.[9] to three-dimensional (3D) and named it as a thermal abuse model for TR induced by heating. The heat generated by the electrolyte decomposition reaction was added to the source term. They studied the effect of cell size and surface to volume ratio and hot spot propagation inside the cell. The thermal abuse model has since been widely used to predict the thermal behaviour of LIBs under heating conditions.[12-23] Peng et al.[12] numerically investigated TR of LIBs with different cathodes. Esho et al.[14] adopted both single and multiple reactions to predict the maximum threshold temperature. Huang et al.[15, 24] further analysed the criticality of TR of LIBs using the Semenov and Thomas model. Coman et al.[13, 25] incorporated venting into the thermal abuse model and developed both lumped and three-dimensional (3D) models considering the state of charge for predicting TR of cylindrical cells. Feng et al.[26] developed a TR model coupled short circuit and chemical reaction. In addition, some researchers considered the reversible and the irreversible heat effects as well as chemical reactions in the heat source term to predict the thermal behaviour of LIBs under charge/discharge conditions[9, 20, 22, 27, 28] or overcharge conditions.[29, 30] Guo et al.[27] developed a 3D model with the reversible and the irreversible heat generation and compared the model predictions with oven test. An et al.[22] proposed an analytical TR model

using the nominal heat generation calculated from an electrochemical-thermal coupled model. Lee et al.[28] further incorporated both the electrochemical model and the short-circuit model into the thermal abuse model. Ren et al.[29] and Qi et al.[30] investigated the TR behaviour of LIBs under overcharge using a modified electrochemical-thermal coupled model. Recently, the thermal abuse model has been extended and used in the TR propagation model.[18, 24, 26, 31] The TR propagation behaviour of cylindrical LIBs[18] and pouch LIBs[31] were numerically investigated.

The chemical reactions during TR are overlapped and temperature-dependent.[32, 33] To separate the overlapped reaction peaks into individual reaction peaks, Ping et al.[33, 34] proposed a deconvolution method to study the thermal behaviour of battery components and full cells. The kinetic parameters for the individual reaction were easily estimated based on the Arrhenius equation. Ren et al.[35] measured the heat flow of battery components used differential scanning calorimetry (DSC) and determined six dominant exothermic reactions. They also developed a TR model which coupled all dominant exothermic reactions. Liu et al.[36] also used DSC to get 11 chemical reactions of battery components and developed a model coupled with electrochemical behaviour.

Many models have been proposed to predict battery temperatures under thermal abuse conditions. All models are based on the Arrhenius equation with a lot of input parameters needed to be determined such as kinetic parameters and reaction order. Usually, many experiments such as DSC are necessary to obtain these parameters accurately. These experiments are time-consuming and costly. In our previous study, the kinetic parameters for individual chemical reactions at different stages were estimated based on the relationship between the rate of temperature rise and temperature rise. Based on obtained kinetic parameters, a predictive approach has been developed to predict the electro-thermal response of LIBs from

normal to abuse conditions using open-source CFD code OpenFOAM.[37] However, the developed approach requires a relatively larger number of input parameters for the heat source.

To overcome this limitation, the present study proposes a simplified mathematical model with a reduced number of input parameters to facilitate the prediction of TR evolution in LIBs without the need to disassemble them to measure the thermal response of cell components by DSC or other calorimeters to obtain the kinetic parameters. The necessary input parameters for the model can be provided with ARC tests and previous studies. A series of tests have also been conducted for 21700 cells to aid model validation. The model was firstly verified with the measured cell surface temperature evolution and TR trigger time in the ARC tests and then applied to uniform heating tests with two different heating methods specifically conducted to facilitate model validation. Finally, exploratory studies were conducted to investigate the critical ambient temperature that triggers cell TR. Although TR behaviour can also be influenced by lithium plating caused by overcharging[29, 30, 38] and fast charging[39-42], the present study is focused on TR induced by overheating.

2. Mathematical model

The present model has been formulated as three-dimensional (3D), 2D axisymmetric and 0D lumped models to facilitate efficient and accurate numerical simulations in different conditions.

2.1. Three-dimensional model (3D)

The energy balance equation of the cell in Cartesian coordinates can be written as[43]:

$$\rho C_p \frac{dT}{dt} = \frac{\partial}{\partial x}\left(k_x \frac{\partial T}{\partial x}\right) + \frac{\partial}{\partial y}\left(k_y \frac{\partial T}{\partial y}\right) + \frac{\partial}{\partial z}\left(k_z \frac{\partial T}{\partial z}\right) + \frac{\dot{Q}_{\text{gen}}}{V} \tag{1}$$

where ρ denotes the density of the cell, C_p the specific heat capacity, T the temperature, t the time, k_x, k_y, and k_z the thermal conductivities of the cell in x, y, and z directions, respectively,

V the volume of the cell, and $\dot{Q}_{\text{gen}}$ the heat generation rate. In cylindrical coordinates, the energy balance equation is written as:

$$\rho C_p \frac{dT}{dt} = \frac{1}{r}\frac{\partial}{\partial r}\left(k_r r \frac{\partial T}{\partial r}\right) + \frac{1}{r^2}\frac{\partial}{\partial \varphi}\left(k_\varphi \frac{\partial T}{\partial \varphi}\right) + \frac{\partial}{\partial z}\left(k_z \frac{\partial T}{\partial z}\right) + \frac{\dot{Q}_{\text{gen}}}{V} \tag{2}$$

where k_r, k_φ, and k_z are the thermal conductivities of the cell in r, φ, and z directions, respectively.

The cell initial temperature is assumed to be the same as the measured cell surface temperature:

$$T = T_0 \tag{3}$$

where T_0 is the initial temperature of the cell. The boundary conditions of the cell can be expressed by

$$-\boldsymbol{n} \cdot \boldsymbol{q} = h(T_\infty - T) + \varepsilon\sigma(T_\infty^4 - T^4) \tag{4}$$

where $\boldsymbol{n}$ and $\boldsymbol{q}$ are the normal vectors on the boundary and the conductive heat flux vector, respectively, h is the heat transfer coefficient, ε is the surface emissivity, σ is the Stefan-Boltzmann constant, and T_∞ is the surrounding temperature. For vertical cylinder under natural convection, h is given by[44]:

$$h = \begin{cases} 1.485088 \left|\frac{T_\infty - T}{H_{\text{cell}}}\right|^{0.25}, H_{\text{cell}} > 0.152 \text{ m} \\ 0.941145 \left|\frac{T_\infty - T}{H_{\text{cell}}}\right|^{0.35}, H_{\text{cell}} < 0.152 \text{ m} \end{cases} \tag{5}$$

where H_{cell} is the height of the cylindrical cell.

2.2. 2D axisymmetric model (2D)

If the cell geometry, boundary conditions, material properties, and heat sources are symmetric about an axis z, the temperature within the cell changes with the radial and axial

distances r and z and time t. Therefore, the energy balance equation of the cell in cylindrical coordinates can be simplified as:

$$\rho C_p \frac{dT}{dt} = \frac{1}{r}\frac{\partial}{\partial r}\left(k_r r \frac{\partial T}{\partial r}\right) + \frac{\partial}{\partial z}\left(k_z \frac{\partial T}{\partial z}\right) + \frac{\dot{Q}_{gen}}{V} \tag{6}$$

The initial value and boundary conditions are the same as the three-dimensional model.

2.3. Lumped model (0D)

The lumped model (0D) can be adopted if the Biot number satisfies the following condition [45]

$$Bi = hL_c/k < 0.1 \tag{7}$$

where L_c is the characteristic length, k is the thermal conductivity. If the cell meets the above condition, it indicates that the temperature gradient within the cell is small.[45] Hence, the energy balance equation can be simplified as

$$C_p m_{\text{cell}} \frac{dT_{\text{cell}}}{dt} = \dot{Q}_{\text{gen}} + \dot{Q}_{\text{diss}} \tag{8}$$

where m_{cell} and V_{cell} are the mass and volume of the cell, respectively, and $\dot{Q}_{\text{diss}}$ heat dissipation considering both convection and radiation heat transfer expressed as for the whole computational domain:

$$\dot{Q}_{\text{diss}} = A_{\text{cell}}[h(T_\infty - T_{\text{cell}}) + \varepsilon\sigma(T_\infty^4 - T_{\text{cell}}^4)] \tag{9}$$

where A_{cell} is the surface area of the cell,

2.4. Heat source

In generally, the heat generation rate of the cell without charging/discharging during TR is given by[2, 25],

$$\dot{Q}_{\text{gen}} = \dot{Q}_{\text{SEI}} + \dot{Q}_{\text{An-Ele}} + \dot{Q}_{\text{Ca-Ele}} + \dot{Q}_{\text{Ele}} + \dot{Q}_{\text{ISC}} \tag{10}$$

9

where $\dot{Q}_{SEI}$ is the dominant heat generation rate (HGR) of SEI decomposition, $\dot{Q}_{An-Ele}$ the dominant HGR from the reaction of intercalated lithium at the anode with electrolyte, $\dot{Q}_{Ca-Ele}$ the dominant HGR from the reaction of the cathode material with electrolyte and the reaction of emitted oxygen generated by the cathode material decomposition with electrolyte, $\dot{Q}_{Ele}$ the dominant HGR from the electrolyte decomposition, the reaction of electrolyte with electrode material and binder, and $\dot{Q}_{ISC}$ the Joule heat generated by ISC. Here, a simplified model of heat generation rate is considered by dividing the whole process of heat generation into two stages. The main heat generation rate at the first stage denoted by $\dot{Q}_I$ is generated by SEI decomposition and the reaction of intercalated lithium at the anode with electrolyte, and the main heat generation rate at the second stage denoted by $\dot{Q}_{II}$ is generated by the electrolyte decomposition, the cathode material decomposition, the reaction of electrolyte with electrode material and released oxygen and ISC. At stage II, the flammable electrolyte/combustible gases can be ignited by a large amount of oxygen released from the cathode material decomposition at high temperatures.[46, 47] The heat generation rate at the first stage is small compared to the second stage. The reaction at the second stage is considered to be autocatalytic[48], namely, the initial reaction is slowly but accelerates rapidly at the final stage. The heat generation rate can be written as

$$\dot{Q}_{gen} = \dot{Q}_I + \dot{Q}_{II} \tag{11}$$

where $\dot{Q}_I$ and $\dot{Q}_{II}$ are calculated as[9, 48]

$$\dot{Q}_I = -m_I H_I \frac{dc}{dt} \tag{12}$$

$$\frac{dc}{dt} = -A_I \exp\left(-\frac{E_I}{RT}\right) c \tag{13}$$

$$\dot{Q}_{II} = m_{II} H_{II} \frac{d\alpha}{dt} \tag{14}$$

10

$$\frac{d\alpha}{dt} = A_{\text{II}}\exp\left(-\frac{E_{\text{II}}}{RT}\right)(1-\alpha)^n \tag{15}$$

where m_i (i=I and II) denotes the mass of the reactant, H_i the reaction heat per unit mass, c the normalised amount of the reactant with an initial value of 1, α the fractional degree of conversion with an initial value of 0, A_i the pre-exponential factor for the reaction, E_i the activation energy for the reaction, n the reaction order, and R the universal gas constant. Figure 1 shows a schematic of modeling parameters acquisition and a comparison of the numbers of parameters needed and the mathematical model between the present method and the previous method. The present TR model only needs 12 parameters, which are half the parameters taken by Kim et al.[11]. The determination of these parameters and the division of two stages will be introduced in Section 4.1. The proposed model differs from the previous thermal abuse model of Kim et al.[11] mainly shows that the exothermic reactions in whole TR process are described by two Arrhenius equations as shown in Eqs. 13 and 15. The main advantage of this model is its simplicity for implementation into different CFD or multi-physics codes as fewer parameters need to be determined and there is no need to determine the initial value of the normalized amount. It should be noted that the present model generally divides the whole overlapped exothermic reactions into two dominant chemical reaction stages, but it does not clearly distinguish a sequence of reactions inside cell. It also neglects the effect associated with the change of SEI thickness.[9] As a result, this model is not suitable to predict the change of SEI thickness and reaction sequence of battery components. It should be added that, although the simplified model with the parameters to be determined in the Section 4.1. is developed for the prediction of thermal runaway of commercial cylindrical 21700 cells, the developed modelling approach is generic and can be extended to other LIBs with different types and cathode materials.

2.5. Model implementation

The governing equations, boundary conditions, and initial values of the three-dimensional model, the 2D axisymmetric model, and the lumped model are presented in Fig. 2. To verify the present model, a series of tests under various heating conditions are conducted. The key kinetic parameters are estimated based on the best fit of data from one ARC test. The derived parameters and their implementation in the code are then verified with a different set of ARC test data. Validation studies are then conducted by comparing predictions with measurements in cell heating tests by flexible and nichrome wire heaters. Finally, the validated model is applied to investigate the critical ambient temperature. The lumped model (0D) can be used for predicting ARC tests and the critical ambient temperature prediction when the Biot number is less than 0.1 for cell surface temperature below 528 °C and around 0.1 for cell surface temperature between 528 °C and the maximum measured temperature. The 2D axisymmetric model (2D) is used for predicting ARC tests, nichrome wire heater test and the critical ambient temperature prediction as the applied heating conditions are axisymmetric. The 3D model is used for predicting flexible heater tests because the heater is not axisymmetric.

The model has been implemented in COMSOL Multiphysics 5.4® and used in all simulations. As shown in Fig. 2, both 2D model and 3D model consider the complex battery structure. Nitrogen is assumed to fill in the mandrel and gap between safety devices and jelly roll, and the void of top cover and safety devices is filled with air. The material of the top cover and safety devices is assumed to be the same as the steel can. Properties of jelly roll and steel can are listed in Table 1 while other material properties are from COMSOL material library. A uniform volume heat source is considered because the jelly roll is heated uniformly. Accordingly, the average value of all nodal temperatures in jelly roll region is used to calculate the reaction heat. The power of the external heater is applied as a boundary heat source. The implicit backward differentiation formula (BDF) solver with five orders of accuracy, fixed time

step and the fully coupled approach are used in all simulations. Noting that the solver will take very small time steps when the model is approaching the maximum temperature, it means that the solver will use the adaptive time steps not the given fixed time step when the rate of temperature rise is changing rapidly.

3. Experimental setup

Commercial cylindrical 21700 LIBs with Ni-rich $Li(Ni_xMn_yCo_z)O_2$ cathodes were chosen for the present study. The capacity and nominal voltage of the cell are 5 Ah and 3.63 V, respectively. The cells were fully charged at 1455 mA to 4.2 V, followed by end current 50 mA (4.2V) before the tests. As shown in Fig. 3a, extended volume accelerating rate calorimeter (EV-ARC) was used to study the TR behaviour of these cells. A tracking thermocouple (Fig. 3d) was positioned in the centre of the cell and held on with high-temperature insulated tape and an aluminium band. An open throne was used to hold the cell in an upright position and prevent it from being fired across the EV-ARC chamber during the test. Figures 3b and 3c show that an external heat source was attached to the outside of the cell casing, which was clamped vertically by a metal clamp and wrapped with 1 cm of insulation tape around the bottom of the casing to prevent heat loss to the metal clamp. The clamp was fixed on a wall. Two kinds of external heaters were used in tests. One is a flexible heater 2'' by 2'' with a resistance of 17.9 Ω (KHLVA-202/10-P, Omega). Another heater is made of an enamelled nickel chrome wire 0.25 mm thickness with a resistance of 23.9 Ω (NC0250EN-010m, Scientific Wire Company). The plastic wrap of cell tore off before sticking on the cell casing. The length of the cell inserting the clamp was about 12.5 mm shown in Figs. 3e and 3f. The enamelled nichrome chrome wire was wrapped 15 times around the cell, with a 2.5 mm gap between each turn. It was secured to the cell casing with double-sided Kapton tape and had taps soldered on to each end to provide power. The thermocouples located at the side centre of cell not covered by the flexible heater (Fig. 3e) and at the side of cell 7 cm from the top (Fig.

3f), respectively. All cells in tests were fully charged and heated to failure by external heaters. Fan ventilation was switched on after cell ignition and at the same time, the external heater was turned off. The temperature on the cell surface and the voltage of some cells were measured during tests. The test configurations and parameters are summarized in Table 2.

4. Results and discussion

4.1. EV-ARC tests and kinetic parameters estimation

Test settings followed the standard ARC heat-wait-seek protocol with the cell in an open configuration. The heat-wait-seek method was adopted because it could be easily realized in the present model. The cell was in an almost adiabatic environment and the onset self-heating temperature of the cell was easily obtained using this protocol. The starting temperature was specified as 50°C, and the maximum test temperatures 300.00 °C for Test 1 and 350.00 °C for Test 2, respectively. The temperature increase step was 5 ºC and temperature rate sensitivity 0.02 °C/min. The waiting time was 30 minutes for Test 1 and 25 minutes for Test 2 plus the 10 minutes seek period after the wait time in which the ARC looks for exothermic activity in the sample. The mass of cell in Test 1 and Test 2 was 68.74 g and 68.20 g, respectively. The specific heat capacity of the cell considers the same value as the jell roll. The surface emissivity is 0.8.[9] The geometric parameters of the cell are summarised in Table 3. A total of 5060 triangles for the 2D model is adopted based on mesh independence tests. The fixed time step 0.02 min was used considering calculation efficiency and accuracy.

The curve of the rate of temperature rise versus temperature on the cell surface was divided into two stages as described in Section 2.4. The reaction order at stage II is taken as 7.5, which is fitted to match the maximum rate of temperature rise. As shown in Fig. 4a, the temperature range of stage I is between 88 ºC (the onset temperature of cell self-heating detected by EV-ARC denoted by T_1) and 143 ºC (the minimum rate of temperature rise after peak value denoted by T_2), and the temperature range of stage II is from T_2 to the maximum temperature T_{max}.

According to the energy balance equation under adiabatic condition, the total heat produced by exothermic reaction per unit mass H_i (i=I and II) is given by[48-50]

$$H_i = \eta C_p \Delta T \tag{16}$$

where η is a modification factor, and ΔT is the adiabatic temperature rise. For the stage I, $\eta = 1$ and $\Delta T = 55$ K ($T_2 - T_1$). For stage II, $\eta = 1.136$, which is fitted to match the maximum temperature because the reactants are not completely converted to products at this stage in the numerical simulation due to numerical tolerance and $\Delta T = T_{max} - T_2$. It should be noted that it is assumed that the reactants are completely converted to products at the stage II, namely $\eta = 1$, in the calculation of Eq. (17). The mass of the reactant m_i is set to be the same as the mass of the cell. Combining the Eqs. 8, 14 and 15, the following relation can be obtained as

$$\frac{dT_{cell}}{dt} = A_{II}(T_{max} - T_2)\exp\left(-\frac{E_{II}}{RT_{cell}}\right)(1 - \alpha)^n \tag{17}$$

Considering α is approximately equal to 0 at the beginning of stage II, that is, the degree of conversion of reactant is initially negligible, the final relation for estimating the kinetic parameters can be given by[48, 50]

$$\ln\left(\frac{dT_{cell}}{dt}\right) \approx \ln[A_{II}(T_{max} - T_2)] - \frac{E_{II}}{RT_{cell}} \tag{18}$$

The plot of $\ln(dT/dt)$ versus $1/T$ of Test 1 at the stage II is shown in Fig. 4b, hence the kinetic parameters of stage II can be obtained. The activation energy at the stage I was taken from references[9, 11, 16] because it was widely used and validated in LIBs with carbon-based anode. The pre-exponential factor at the stage I was estimated by fitting the test data of temperature versus time in Test 1. Table 4 shows the derived kinetic parameters for the model. The

The experimental measurements and predictions of the EV-ARC tests are compared in Figs. 4c-4f. Average temperatures of calorimeter temperatures on the inner surface of the top, side, and bottom zones in the EV-ARC chamber were used as input ambient temperatures before the

temperature on cell surface reached the onset temperature of cell self-heating detected by EV-ARC. After that, the adiabatic condition was considered until the temperature on cell surface exceeded the given maximum test temperatures. As shown in Fig. 4c, the predictions using the 0D lumped model and 2D axisymmetric model match well with the measured temperatures in Test 1. As shown in Table 5, the predicted maximum temperatures on the cell surface were 758.7 °C (0D) and 759.9 °C (2D), which was slightly lower than the measurement of 762.1 °C. The predicted time to reach the maximum temperature was 1446.2 min (0D) and 1441.3 min (2D), which was very close to the measurement of 1446.2 min. The repeated test was conducted to validate the effectiveness of estimated kinetic parameters and the proposed model. As shown in Fig. 4d, the predictions in the lumped model (0D) and 2D axisymmetric model (2D) both agree well with the experimental measurements in Test 2. The predicted maximum temperature on the cell surface was 697.7 °C (0D) and 705.2 °C (2D). Both were in reasonable agreement with the measured value of 710.7 °C. The predicted time to reach the maximum temperature was 1382.3 min (0D) and 1385.2 min (2D), both were only slightly higher than the measurement of 1380.7 min. These results indicate that the proposed model with the estimated kinetic parameters can well capture the thermal behaviour of 21700 cells. Figures 4e and 4f show a comparison of the predicted and measured rates of temperature increase. The predictions agree well with the test data for the lumped model (0D) and the 2D axisymmetric model (2D) before 197 °C, but larger than the measurements after around 197 °C. The possible reason is that the time step becomes adaptive and is much smaller than the sampling interval of the thermocouple when cell temperature changes quickly. Large temperature rise at a very small time step will cause a huge change in the rate of temperature rise and hence the discrepancy between the predicted and measured rate of temperature rise in this period is relatively large.

4.2. Thermal runaway of the cell under heating by the flexible heater

Three tests with different initial and ambient temperatures were performed. As mentioned earlier, the 3D model is used for these predictions as the heater is not axisymmetric. The real powers of flexible heaters were not the same. As shown in Fig. 5a, the heaters were turned on at different times and turned off after cell ignition. The power of the heater remained almost constant until the heater was turned off. The thermal boundary conditions are shown in Fig. 3e. The clamped part of the cell was thermally insulated while the other boundaries are subject to both convective and radiative heat transfer. The effective average heater power obtained by fitting the temperature versus time in the tests was 0.745 times the average heater power. This value was used as input until the average temperature of the cell reached the maximum temperature, then the fan ventilation was activated, and the forced convective heat transfer coefficient was set to 130.0 W m^{-2} K^{-1} to match the experimental results while the recommended typical value is 200 W m^{-2} K^{-1} for moderate speed cross-flow of air under forced convection.[51] A total of 28810 tetrahedra, 1828 pyramids, 9504 prisms and 30162 hexahedra for the 3D model is adopted based on mesh independence tests. The fixed time step was 0.2 s in these three cases considering calculation efficiency and accuracy. As shown in Table 5, the predicted and measured thermal runaway time are in excellent agreement with the largest discrepancy being less than 1.5%. Relatively larger discrepancies are found between the predicted and measured maximum cell surface temperatures. This might have been caused by the relatively looser contact between the thermocouple and the cell surface after TR.

Figures 5b-5d present a comparison between the measurements and predictions for Tests 3-5. The measured temperature in Test 3 decreased sharply after reaching the maximum since the thermocouple became completely detached from the cell. The predicted temperatures in Test 4 were in good agreement with the measurement. The predicted time to TR in Test 5 was only a few seconds later than measurement and the temperatures were only slightly higher than the

17

measurements before reaching the maximum temperature. For Test 4, the recorded voltages were not greater than 0.1 V, indicating that the voltage measurement was problematic, and hence it was not plotted in Fig. 5c.

Figure 6 shows the temperature contours of the shell case and cross-section at the middle height of the cell for Test 4 at different times. Several typical stages can be presented: pre-heat stage (Fig. 6b), thermal runaway stage (Figs. 6c-6d), and cooling stage (Fig. 6e). Temperatures on cell surface keep increasing until reaching the maximum and drops quickly after that due to forced convection caused by the fan. Temperatures inside the cell are less than that on the surface at the pre-heat stage and much higher than them after that. It should be noted that temperatures of top cover are always lower than other parts in simulation because hot gas release after breakage of safety value and possible fire after thermal runaway are not considered. But the net accumulated heat of cell is considered when calculating the reaction heat.

4.3. Thermal runaway of the cell under heating by the nichrome wire

The nichrome-wire heater was used to heat the cell to failure. The heater was turned on at 5.8 s and turned off after cell ignition. The power of the heater almost kept unchanged until the heater was turned off. The effective average heater power is 14.584 W, which is 0.722 times the average heater power of 20.2 W. The boundary conditions are shown in Fig. 3f. The clamped part of the cell was thermally insulated while the other parts are subject to both convection and radiation. The 2D axisymmetric model was adopted and the fixed time step 0.2 s was used in the simulation considering calculation efficiency and accuracy.

As shown in Figs. 7a and 7b, the predictions agree well with the measurements before 180 °C while there are some discrepancies afterwards. The predicted time for the cell surface temperature to reach 180 °C is 1198.8 s, which is very close to the measured value of 1198.2 s. The predicted maximum temperature on the cell surface is 555.0 °C, which is slightly larger

than the measurement of 517.9 °C. The time for cell surface to reach the maximum temperature is, however, in reasonably good agreement with the measurements with the discrepancy being around 1%. Figure 7b shows the rate of temperature rise in the test and prediction. The predictions fluctuate gently, i.e. less than 2.0 °C/s, and are quantitatively in agreement with the measurements before reaching 180 °C. However, relatively larger discrepancies are observed afterwards. The peak rate of temperature rise for prediction is about 6.5 times measured value. This might be attributed to the same reasons as discussed earlier. The time step becomes adaptive and is much smaller than the sampling interval of the thermocouple when cell temperatures change quickly. As a result, the predicted rate of temperature rise changes rapidly for small temperature rise at a very small time step. The discrepancy might be partially caused by the predicted rapid conversion of reactants, which leads to higher temperature rising rate in the prediction. In addition, the looser contact between the thermocouple and the cell mentioned in Section 4.2 might also have contributed to this discrepancy. The variation of the normalised amount of the reactant with time and the average temperature of the jelly roll is shown in Figs. 7c and 7d. The normalised amount of reactant at the stage I changes from 1 to 0, meaning the reactants are completely consumed during TR. While the fractional degree of conversion at the stage II changes from 0 to 0.9, it indicates that the reactants are not completely converted to products during TR, which is the reason we use a correction factor to increase the reaction heat at this stage. The reactants are converted to products very quickly with a rapid increasement of the degree of conversion from 0.042 to 0.879 in less than 25.6 s, and at the same time the average temperature of the jelly roll changes from 201.8 °C to 683.4 °C (Fig. 7d) and the surface temperature from 179.6 °C to 555.0 °C (Fig. 7a). Figure 8 presents the temperature contours of the cell at different times. The heat contributing to the temperature rise of the cell is mainly from the nichrome-wire heater before 393.4 s. After that, both the heater and chemical reactions contribute to the rise of the cell temperature, which can be found from the

19

consumption of reactants shown in Figs. 7c and 7d; then the heat contribution from chemical reactions dominate after 1198.8 s. The error of temperature on cell surface between test and prediction is within 2% between 393.4 s and 1198.8 s. The cell reaches the maximum temperature in less than 25.3 s and then enters the cooling stage. The temperature inside the cell is higher than that on the cell surface since the chemical reaction dominates inside the cell until the cell surface temperature is the same as the ambient temperature.

4.4. Prediction of the critical ambient temperature triggering cell TR

Based on the above studies, the influence of ambient temperature on the TR of the cell was numerically investigated. The cell was assumed to be fully charged and its initial temperature was 20 °C. The cell was put into a target ambient temperature and kept the ambient temperature unchanged during simulations. The mass of cell was assumed the same as Test 1. The boundary conditions were the same as the ARC numerical cases (Fig. 3d). The lumped model (0D) was adopted and the fixed time step 0.5 s was used in the following numerical cases considering calculation efficiency and accuracy.

Figure 9a presents the temperature curves at different ambient temperatures using the 0D model. The cells go into TR when the ambient temperature is greater than 128 °C and fail to trigger TR below 127 °C. There is a critical ambient temperature to trigger the TR. The time to maximum temperature on the cell surface (TR time) versus the ambient temperature is shown in Fig. 9b. The TR time decreases exponentially with the ambient temperature. The higher the ambient temperature is, the more prone to TR the cell becomes.

5. Conclusions

A simplified mathematical model for predicting the evolution of heating induced TR of 21700 cells has been developed. This model assumes that the exothermic reactions during TR follow two Arrhenius expression to describe the decomposition reaction and autocatalytic

reaction. These assumptions have reduced the input parameters required to calculate heat generate rates generated by exothermic reactions. The model has been formulated as lumped 0D, axisymmetric 2D and full 3D. The lumped model (0D) can be used for predicting ARC tests and the critical ambient temperature when the Biot number is small, the 2D axisymmetric model is used when the heating conditions are axisymmetric and the 3D model can be used with neither of the above conditions can be met, such as the flexible heater tests in the present study. The model has been implemented in COMSOL Multiphysics 5.4® in the present study, but it can be easily implemented into other CFD codes as well.

Verification was firstly conducted with the newly conducted EV-ARC tests for commercial 21700 LIBs. Following the derivation of the kinetic parameters from the measurements of the first EV-ARC test, the model was used to predict the temperature evolution of the second EV-ARC test. The predicted temperatures with both the 0D and 2D models are in very good agreement with the measurement. The predicted peak temperatures by the 0D and 2D models were within 2% and 1% with the measured value. The predicted time to the maximum temperature by the 0D and 2D models was both within 1% with the measured value.

The model was then validated with heating tests by both flexible heater and nichrome-wire heaters. The variation of the normalised amount of reactant and degree of conversion with time and temperature was used to further explain the change of temperature rising rate of the cell during TR. The model has achieved reasonably good agreement with the measurements for the time to reach the maximum temperature. In addition, the predicted peak value of the rate of temperature rise was much higher than the measurements. The possible reason is that the time step in simulation becomes adaptive when cell temperature changes quickly and is much smaller than the response time of the thermocouple. Finally, the validated model was used to numerically investigate the critical ambient temperature triggering TR. The predicted critical ambient temperature to trigger TR of the type 21700 cell was found to be between 127 °C and

128 °C. The time to TR with maximum surface temperature was found to decrease exponentially with the ambient temperature. It should be mentioned that the developed modelling approach is generic and can be extended to other LIBs with different cathode materials and types in addition to cylindrical cells.

Acknowledgements

References

1. Q. Wang, P. Ping, X. Zhao, G. Chu, J. Sun and C. Chen, *J. Power Sources*, **208**, 210 (2012).

2. X. Feng, M. Ouyang, X. Liu, L. Lu, Y. Xia and X. He, *Energy Stor. Mater.*, **10**, 246 (2018).

3. Q. Wang, B. Mao, S. I. Stoliarov and J. Sun, *Prog. Energy Combust. Sci.*, **73**, 95 (2019).

4. X. Feng, D. Ren, X. He and M. Ouyang, *Joule* (2020).

5. B. Liu, Y. Jia, C. Yuan, L. Wang, X. Gao, S. Yin and J. Xu, *Energy Stor. Mater.*, **24**, 85 (2020).

6. X. Feng, S. Zheng, D. Ren, X. He, L. Wang, H. Cui, X. Liu, C. Jin, F. Zhang and C. Xu, *Appl. Energy*, **246**, 53 (2019).

7.   M. N. Richard and J. R. Dahn, *J. Electrochem. Soc.*, **146**, 2068 (1999).

8.   M. N. Richard and J. R. Dahn, *J. Electrochem. Soc.*, **146**, 2078 (1999).

9.   T. D. Hatchard, D. D. MacNeil, A. Basu and J. R. Dahn, *J. Electrochem. Soc.*, **148**, A755 (2001).

10.   R. Spotnitz and J. Franklin, *J. Power Sources*, **113**, 81 (2003).

11.   G.-H. Kim, A. Pesaran and R. Spotnitz, *J. Power Sources*, **170**, 476 (2007).

12.   P. Peng and F. Jiang, *Int. J. Heat Mass Transf.*, **103**, 1008 (2016).

13.   P. T. Coman, S. Rayman and R. E. White, *J. Power Sources*, **307**, 56 (2016).

14.   I. Esho, K. Shah and A. Jain, *Appl. Therm. Eng.*, **145**, 287 (2018).

15.   P. Huang, H. Chen, A. Verma, Q. Wang, P. Mukherjee and J. Sun, *J. Hazard. Mater.*, **369**, 268 (2019).

16.   C. F. Lopez, J. A. Jeevarajan and P. P. Mukherjee, *J. Electrochem. Soc.*, **162**, A2163 (2015).

17.   L. Zhang, P. Zhao, M. Xu and X. Wang, *Appl. Energy*, **261**, 114440 (2020).

18.   Y. Jia, M. Uddin, Y. Li and J. Xu, *J. Energy Storage*, **31**, 101668 (2020).

19.   S. Abada, M. Petit, A. Lecocq, G. Marlair, V. Sauvant-Moynot and F. Huet, *J. Power Sources*, **399**, 264 (2018).

20.   A. Melcher, C. Ziebert, M. Rohde and H. J. Seifert, *Energies*, **9**, 292 (2016).

21.   A. S. Yeardley, P. J. Bugryniec, R. A. Milton and S. F. Brown, *J. Power Sources*, **456**, 228001 (2020).

22.   Z. An, K. Shah, L. Jia and Y. Ma, *Appl. Therm. Eng.*, **160**, 113960 (2019).

23.   A. Kriston, I. Adanouj, V. Ruiz and A. Pfrang, *J. Power Sources*, **435**, 226774 (2019).

24.   P. Huang, P. Ping, K. Li, H. Chen, Q. Wang, J. Wen and J. Sun, *Appl. Energy*, **183**, 659 (2016).

25.   P. T. Coman, E. C. Darcy, C. T. Veje and R. E. White, *J. Electrochem. Soc.*, **164**, A587 (2017).

26.   X. Feng, L. Lu, M. Ouyang, J. Li and X. He, *Energy*, **115**, 194 (2016).

27.   G. Guo, B. Long, B. Cheng, S. Zhou, P. Xu and B. Cao, *J. Power Sources*, **195**, 2393 (2010).

28.   C. H. Lee, S. J. Bae and M. Jang, *J. Power Sources*, **293**, 498 (2015).

29.   D. Ren, X. Feng, L. Lu, M. Ouyang, S. Zheng, J. Li and X. He, *J. Power Sources*, **364**, 328 (2017).

30.   C. Qi, Y. Zhu, F. Gao, K. Yang and Q. Jiao, *Int. J. Heat Mass Transf.*, **124**, 552 (2018).

31.   S. Bilyaz, K. C. Marr and O. A. Ezekoye, *Fire Technol.*, 1 (2020).

32.   P. Jindal and J. Bhattacharya, *J. Electrochem. Soc.*, **166**, A2165 (2019).

33.   P. Ping, Q. Wang, P. Huang, J. Sun and C. Chen, *Appl. Energy*, **129**, 261 (2014).

34.   Q. Wang, P. Ping, J. Sun and C. Chen, *Thermochim. Acta*, **517**, 16 (2011).

35.   D. Ren, X. Liu, X. Feng, L. Lu, M. Ouyang, J. Li and X. He, *Appl. Energy*, **228**, 633 (2018).

36.   C. Liu, H. Li, X. Kong and J. Zhao, *Int. J. Heat Mass Transf.*, **153**, 119590 (2020).

37.   P. Ping, Q. Wang, Y. Chung and J. Wen, *Appl. Energy*, **205**, 1327 (2017).

38.   W. Mei, L. Zhang, J. Sun and Q. Wang, *Energy Stor. Mater.*, **32**, 91 (2020).

39.   T. R. Tanim, E. J. Dufek, M. Evans, C. Dickerson, A. N. Jansen, B. J. Polzin, A. R. Dunlop, S. E. Trask, R. Jackman and I. Bloom, *J. Electrochem. Soc.*, **166**, A1926 (2019).

40.   J. Sieg, J. Bandlow, T. Mitsch, D. Dragicevic, T. Materna, B. Spier, H. Witzenhausen, M. Ecker and D. U. Sauer, *J. Power Sources*, **427**, 260 (2019).

41.   A. Mistry, F. L. Usseglio-Viretta, A. Colclasure, K. Smith and P. P. Mukherjee, *J. Electrochem. Soc.*, **167**, 090542 (2020).

42.   M. Keyser, A. Pesaran, Q. Li, S. Santhanagopalan, K. Smith, E. Wood, S. Ahmed, I. Bloom, E. Dufek and M. Shirk, *J. Power Sources*, **367**, 228 (2017).

43.   Y. Chen and J. W. Evans, *J. Electrochem. Soc.*, **141**, 2947 (1994).

44.   S.-C. Chen, Y.-Y. Wang and C.-C. Wan, *J. Electrochem. Soc.*, **153**, A637 (2006).

45.   T. L. Bergman, F. P. Incropera, D. P. DeWitt and A. S. Lavine, *Fundamentals of heat and mass transfer*, John Wiley & Sons (2011).

46.   S. Sharifi‐Asl, J. Lu, K. Amine and R. Shahbazian‐Yassar, *Adv. Energy Mater.*, **9**, 1900551 (2019).

47.   M. Parmananda, B. Ryali and P. P. Mukherjee, *J. Phys. Chem. C*, **123**, 30106 (2019).

48.   D. D. MacNeil, L. Christensen, J. Landucci, J. M. Paulsen and J. R. Dahn, *J. Electrochem. Soc.*, **147**, 970 (2000).

49.   B. Mao, P. Huang, H. Chen, Q. Wang and J. Sun, *Int. J. Heat Mass Transf.*, **149**, 119178 (2020).

50.   C.-Y. Jhu, Y.-W. Wang, C.-M. Shu, J.-C. Chang and H.-C. Wu, *J. Hazard. Mater.*, **192**, 99 (2011).

51.   J. H. Whitelaw, *Available http://www.thermopedia.com/content/660/ (Accessed 18 August 2020)* (2011).

52.   J. B. Quinn, T. Waldmann, K. Richter, M. Kasper and M. Wohlfahrt-Mehrens, *J. Electrochem. Soc.*, **165**, A3284 (2018).

53.   P. T. Coman, S. Mátéfi-Tempfli, C. T. Veje and R. E. White, *J. Electrochem. Soc.*, **164**, A1858 (2017).

54.   H. Chen, J. E. H. Buston, J. Gill, D. Howard, R. C. E. Williams, C. M. Rao Vendra, A. Shelke and J. X. Wen, *J. Power Sources*, **472**, 228585 (2020).

Tables

Table 1. Properties of jelly roll and steel can

Parameter	Jelly roll (Measured)	Steel can[9]
k (W m^{-1} K^{-1})	0.998 (radial), 25.8 (axial)	14
C_p (J kg^{-1} K^{-1})	928	460
ρ (kg m^{-3})	2670.3	7917

Table 2. Summary of the test configurations and parameters

External heater	Test no.	Average heater power, P_{avg} (W)	Cell initial temperature, T_0 (°C)	Ambient temperature, T_∞ (°C)
EV-ARC	1	-	24.28	*
	2	-	21.39	*
Flexible heater	3	20.74	28.7	14.6
	4	20.86	9.6	9.1
	5	20.92	11.0	9.9
Nichrome wire	6	20.20	11.7	9.9

* Ambient temperature in the ARC chamber changes with time.

Table 3. Geometric parameters of the type 21700 cell

Parameter	Description	Unit	Value
r_{cell}	Radius of the cell	m	0.0105
H_{cell}	Height of the cell	m	0.07
A_{cell}	Surface area of the cell	m^2	4.9645e-3*
$R_{mandrel}$	Radius of mandrel	m	1.9e-3**
$H_{mandrel}$	Height of mandrel	m	0.0662**
$H_{jellyroll}$	Height of the jelly roll	m	0.0655**
d_{can}	Thickness of the steel can	m	2.0e-4[52]

*The bottom surface area is not included considering to be thermal insulation.

**These values are approximately estimated from a computed tomography scan of type 18650 cell[53] and information from reference.[52]

Table 4. The kinetic parameters for the model

	A_i /s^{-1}	E_i /J mol^{-1}
Stage I	1.124e14 (0D); 9.551e13 (2D/3D)	1.351e5 [9]
Stage II	6.387e11	1.316e5

Table 5. Summary of the experimental measurements and predictions

Test no.	Measured time to maximum temperature (*)	Predicted time to the maximum temperature (*)	Relative error of thermal runaway time	Measured maximum temperature (°C)	Predicted maximum temperature (°C)	Relative error of maximum temperature
1	1446.2	1446.2 (0D)	0.0%	762.1	758.7	-0.4%
		1441.3 (2D)	-0.3%		759.9	-0.3%
2	1380.7	1382.3 (0D)	0.1%	710.7	697.7	-1.8%
		1385.2 (2D)	0.3%		705.2	-0.8%
3	937.8	946.4 (3D)	0.9%	583.5**	623.6	6.9%
4	1063.4	1078.5 (3D)	1.4%	646.9**	621.6	-3.9%
5	1078.4	1083.9 (3D)	0.5%	707.3**	621.2	-12.2%
6	1219.0	1224.0 (2D)	0.4%	517.9	555.0	7.2%

* Unit: min for Tests 1 and 2, s for Tests 3-6.
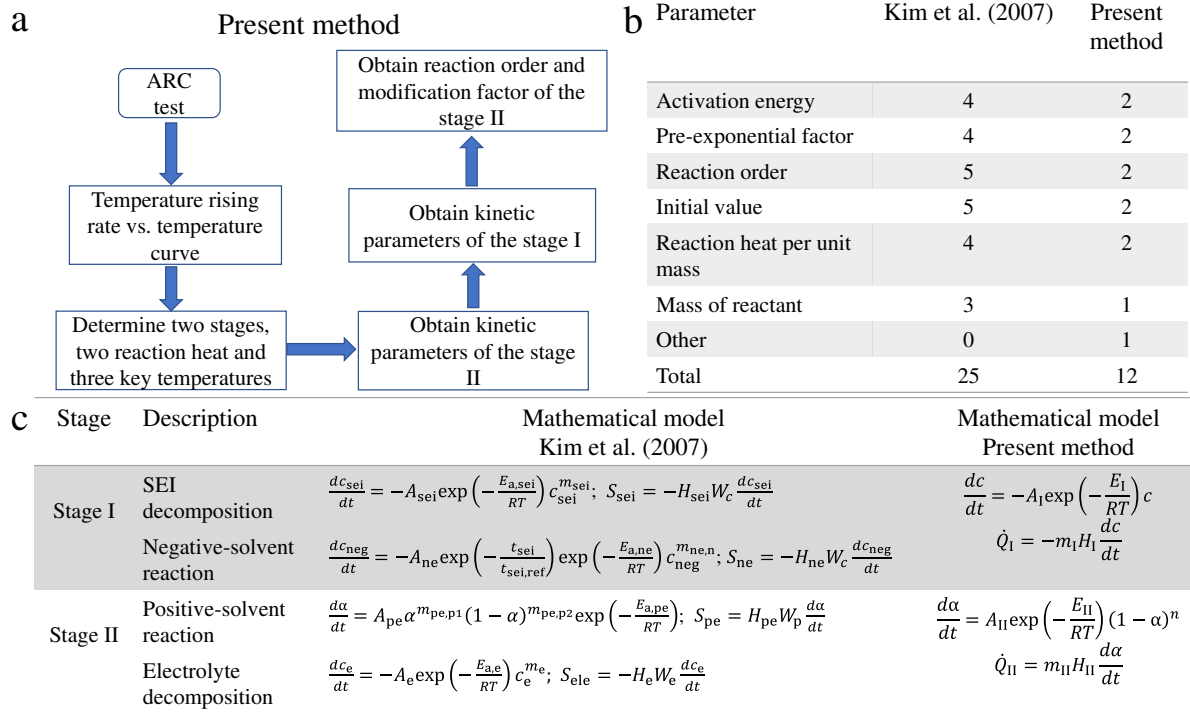
** The maximum temperatures of Tests 3-5 are from Ref.[54]

Figures

a **Present method**

b

Parameter	Kim et al. (2007)	Present method
Activation energy	4	2
Pre-exponential factor	4	2
Reaction order	5	2
Initial value	5	2
Reaction heat per unit mass	4	2
Mass of reactant	3	1
Other	0	1
Total	25	12

c

Stage	Description	Mathematical model Kim et al. (2007)	Mathematical model Present method
Stage I	SEI decomposition	$\frac{dc_{sei}}{dt} = -A_{sei}\exp\left(-\frac{E_{a,sei}}{RT}\right)c_{sei}^{m_{sei}}$; $S_{sei} = -H_{sei}W_c\frac{dc_{sei}}{dt}$	$\frac{dc}{dt} = -A_I\exp\left(-\frac{E_I}{RT}\right)c$ $\dot{Q}_I = -m_I H_I \frac{dc}{dt}$
	Negative-solvent reaction	$\frac{dc_{neg}}{dt} = -A_{ne}\exp\left(-\frac{t_{sei}}{t_{sei,ref}}\right)\exp\left(-\frac{E_{a,ne}}{RT}\right)c_{neg}^{m_{ne,n}}$; $S_{ne} = -H_{ne}W_c\frac{dc_{neg}}{dt}$	
Stage II	Positive-solvent reaction	$\frac{d\alpha}{dt} = A_{pe}\alpha^{m_{pe,p1}}(1-\alpha)^{m_{pe,p2}}\exp\left(-\frac{E_{a,pe}}{RT}\right)$; $S_{pe} = H_{pe}W_p\frac{d\alpha}{dt}$	$\frac{d\alpha}{dt} = A_{II}\exp\left(-\frac{E_{II}}{RT}\right)(1-\alpha)^n$ $\dot{Q}_{II} = m_{II}H_{II}\frac{d\alpha}{dt}$
	Electrolyte decomposition	$\frac{dc_e}{dt} = -A_e\exp\left(-\frac{E_{a,e}}{RT}\right)c_e^{m_e}$; $S_{ele} = -H_eW_e\frac{dc_e}{dt}$	

Fig. 1 (a) A schematic of modeling parameters derivation, (b) comparison of the numbers of required parameters and (c) comparison of the mathematical formulations with that of Kim et al. (2007).
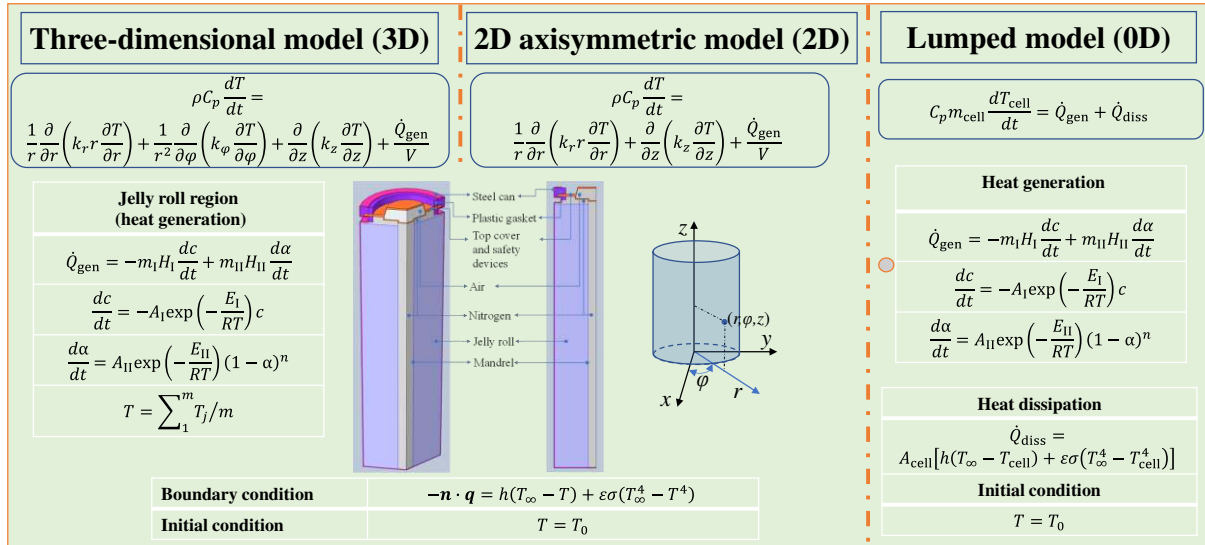
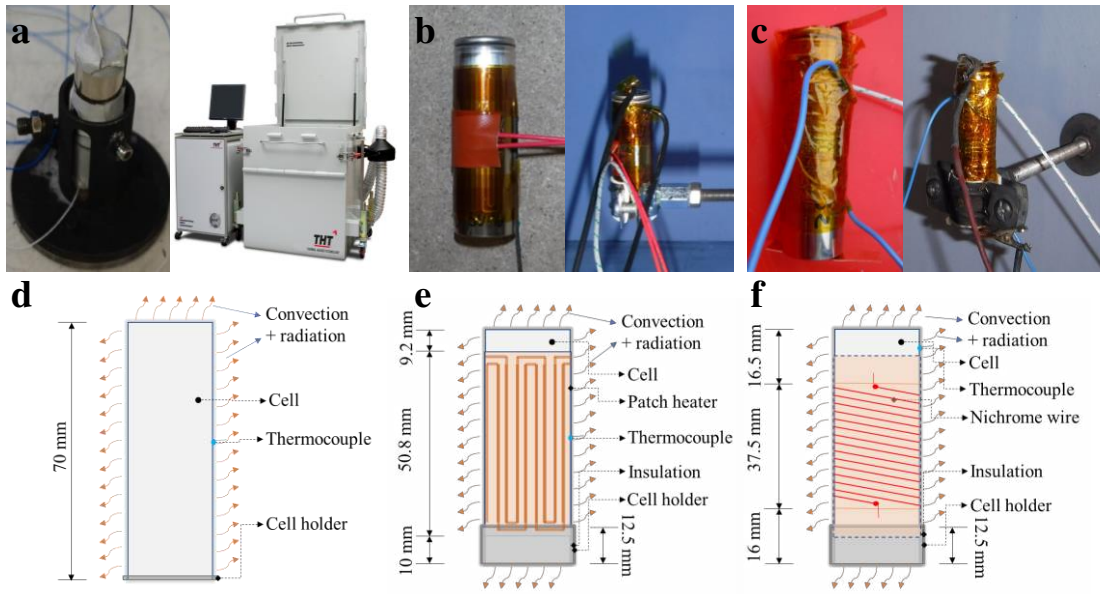Fig. 2. The mathematical model for thermal runaway prediction under heating.

Fig. 3. Schematics of the testing conditions (a) ARC test, (b) flexible heater test, and (c) nichrome wire heater test; 2D sketch of geometrical and boundary conditions for (d) ARC test, (e) flexible heater test, and (f) nichrome wire heater test.
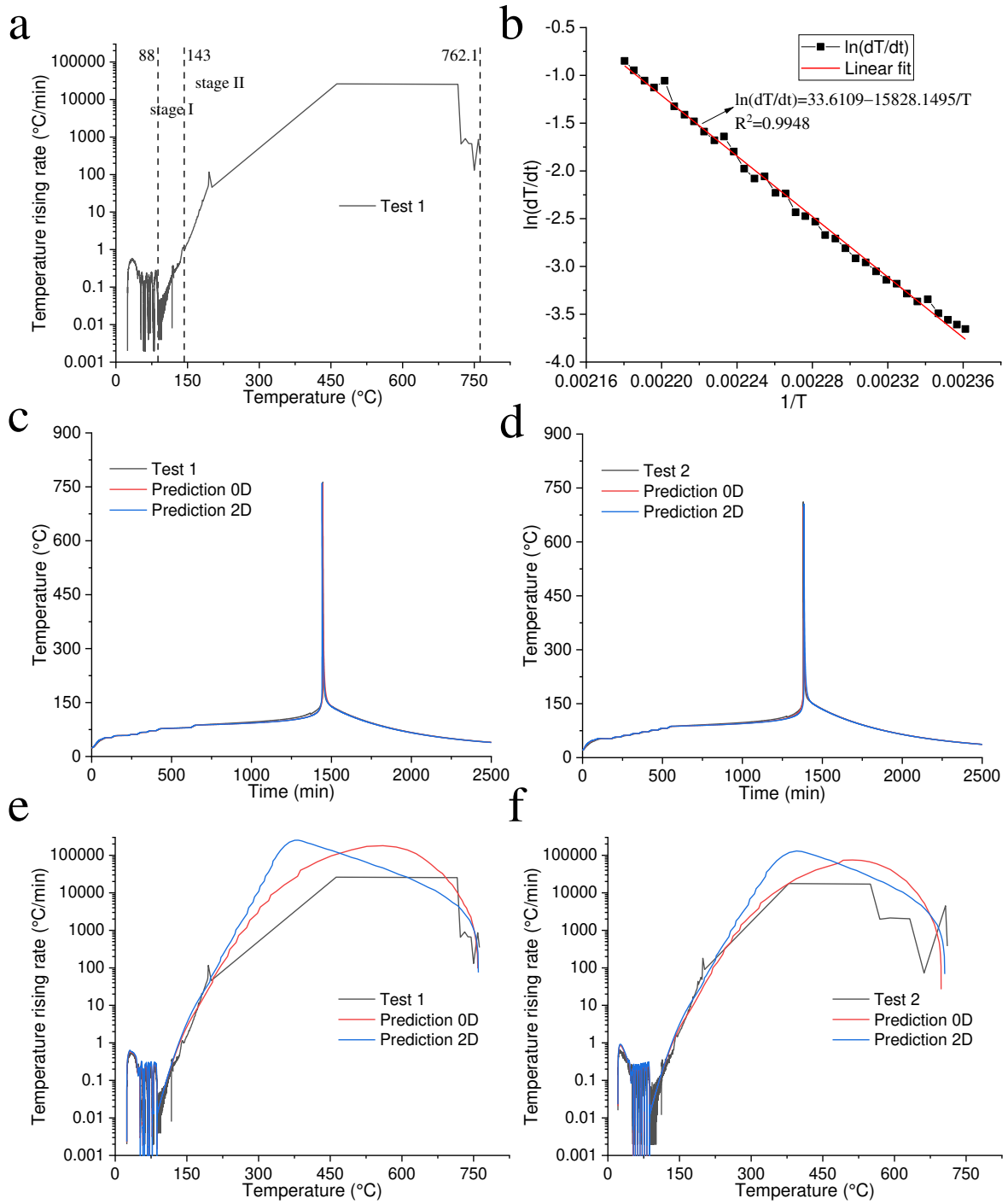
Fig. 4. (a) Stage division of cell self-heating of Test 1, (b) the plot of ln(d*T*/d*t*) versus 1/*T* of

Test 1 at the stage II; cell surface temperatures in (c) Test 1 and (d) Test 2; and the rate of

temperature rise in (e) Test 1 and (f) Test 2.
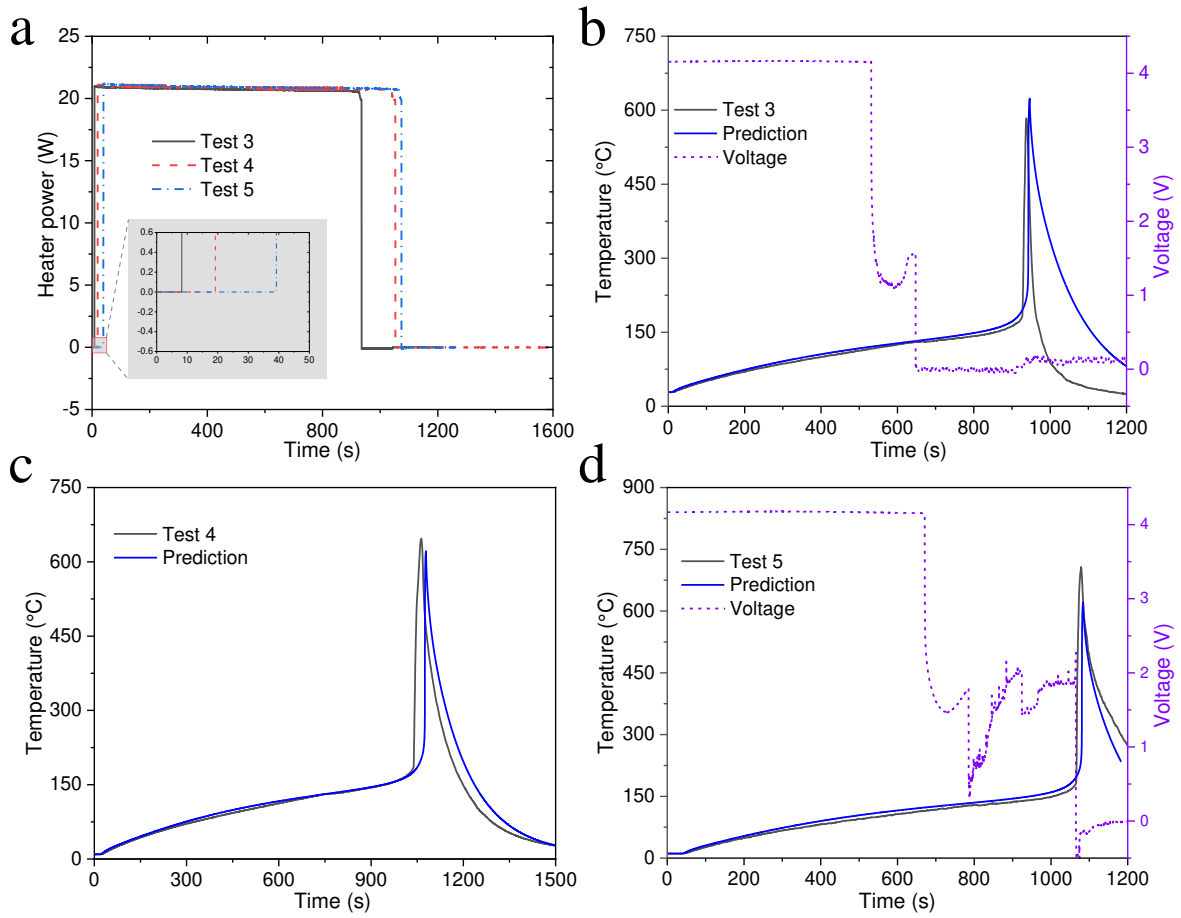
Fig. 5. Comparison between the measurements and predictions for the flexible heater tests.

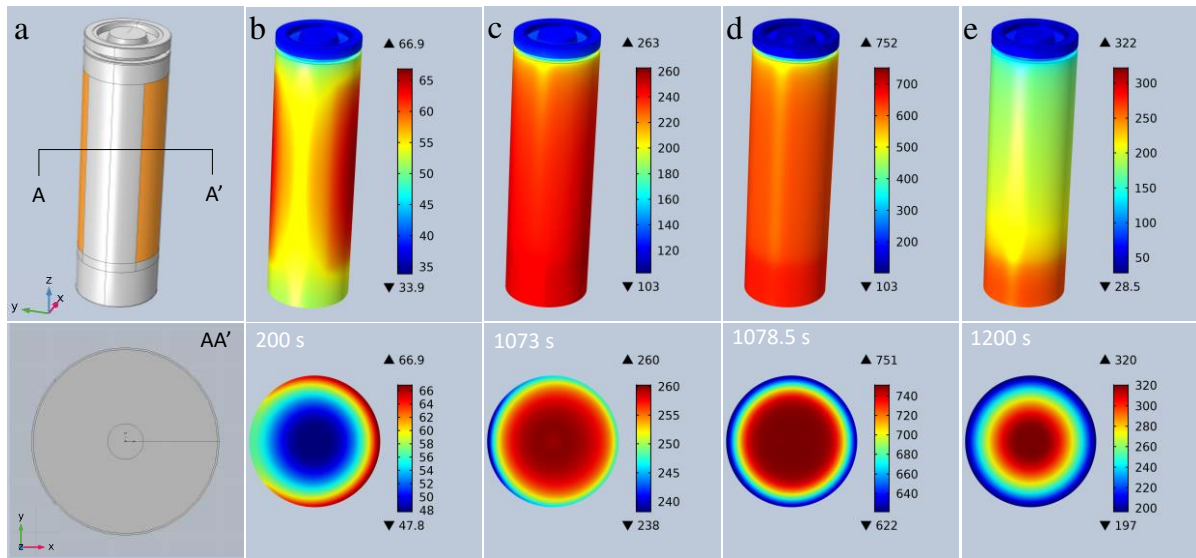(a) Heater power for three tests; Cell surface temperatures in (b) Test 3, (c) Test 4, and (d)

Test 5.

Fig. 6. Temperature contours of the shell case and cross-section at cell middle height for Test 4 at different times. (a) The geometry of the cell and its cross-section, the external heater is marked in yellow, (b) pre-heat stage, (c) a few seconds before thermal runaway, (d) cell with maximum surface temperature, and (e) cooling stage.
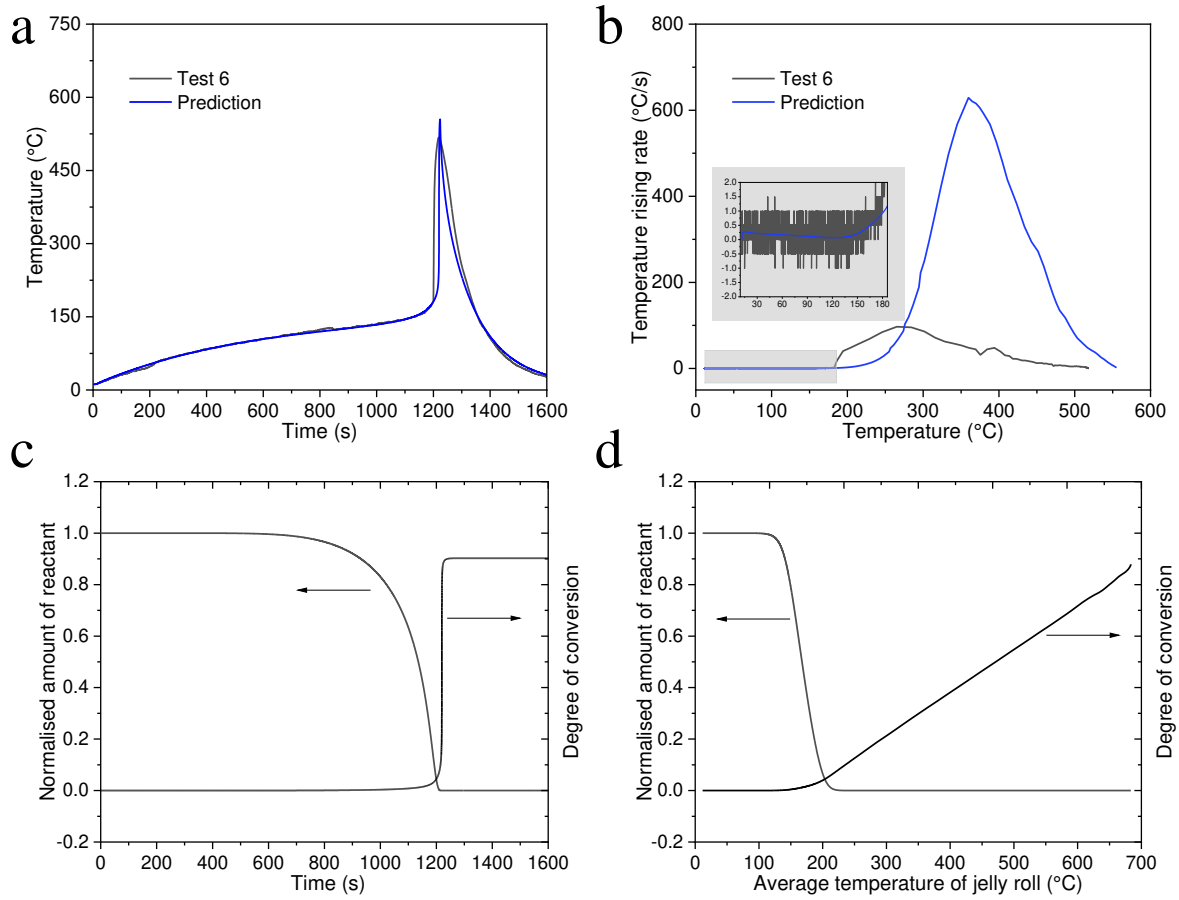
Fig. 7. Comparison between the measurements and predictions for (a) cell surface temperature, (b) temperature rising rate; and variation of the normalised amount of the reactant and degree of conversion with (c) time and (d) average temperature of the jelly roll.
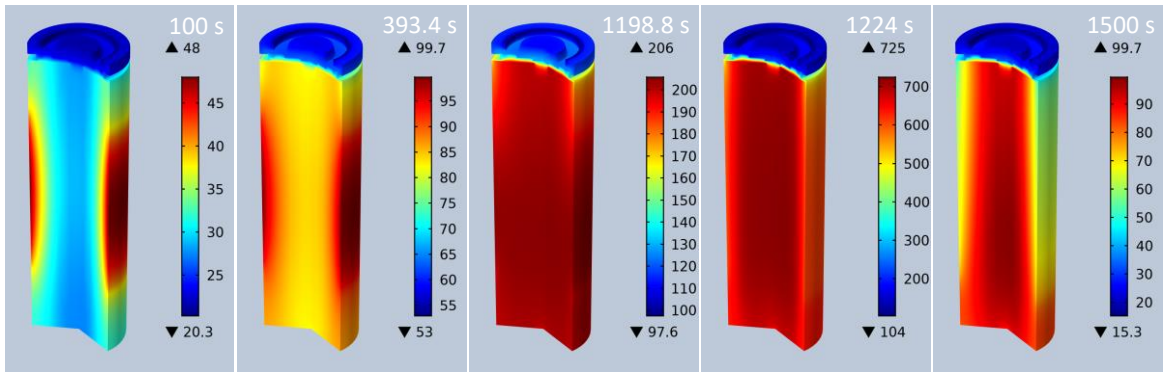
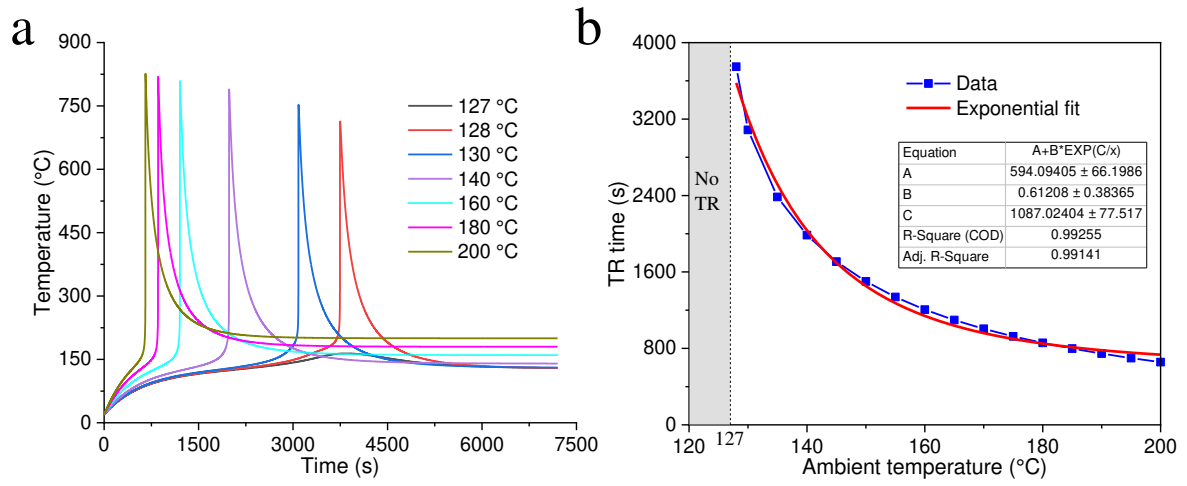Fig. 8. Temperature contours of the cell at different times.

Fig. 9. TR predictions of cells at various ambient temperatures. (a) Effect of ambient temperature, and (b) variation of TR time with ambient temperature.